J Appl Physiol 103: 255–265, 2007.
First published March 29, 2007; doi:10.1152/japplphysiol.01070.2006.

Mechanical basis for lingual deformation during the propulsive phase of swallowing as determined by phase-contrast magnetic resonance imaging

Samuel M. Felton, Terry A. Gaige, Timothy G. Reese, Van J. Wedeen, and Richard J. Gilbert

Department of Mechanical Engineering, Massachusetts Institute of Technology, Cambridge; and the Athinoula A. Martinos Center for Biomedical Imaging, Massachusetts General Hospital, Boston, Massachusetts

Submitted 22 September 2006; accepted in final form 23 March 2007

Felton SM, Gaige TA, Reese TG, Wedeen VJ, Gilbert RJ. Mechanical basis for lingual deformation during the propulsive phase of swallowing as determined by phase-contrast magnetic resonance imaging. *J Appl Physiol* 103: 255–265, 2007. First published March 29, 2007; doi:10.1152/japplphysiol.01070.2006.—The tongue is an intricately configured muscular organ that undergoes a series of rapid shape changes intended to first configure and then transport the bolus from the oral cavity to the pharynx during swallowing. To assess the complex array of mechanical events occurring during the propulsive phase of swallowing, we employed tongue pressure-gated phase-contrast MRI to represent the tissue's local strain rate vectors. Validation of the capacity of phase-contrast MRI to represent local compressive and expansive strain rate was obtained by assessing deformation patterns induced by a synchronized mechanical plunger apparatus in a gelatinous material phantom. Physiological strain rate data were acquired in the sagittal and coronal orientations at 0, 200, 400, and 600 ms relative to the gating pulse during 2.5-ml water bolus swallows. This method demonstrated that the propulsive phase of swallowing is associated with a precisely organized series of compressive and expansive strain rate events. At the initiation of propulsion, bolus position resulted from obliquely aligned compressive and expansive strain, vertically aligned compressive strain and orthogonal expansion, and compressive strain aligned obliquely to the styloid process. Bolus reconfiguration and translocation resulted from a combination of compressive strain occurring in the middle and posterior tongue aligned obliquely between the anterior-inferior and the posterior-superior regions with commensurate orthogonal expansion, along with bidirectional contraction in the distribution of the transversus and verticalis muscle fibers. These data support the concept that propulsive lingual deformation is due to complex muscular interactions involving both extrinsic and intrinsic muscles.

tongue; lingual deformation

THE HUMAN TONGUE IS A VERSATILE and structurally complex muscular organ that is of paramount importance for the performance of swallowing. During the oropharyngeal swallow, a highly synchronized series of events results in the manipulation and transport of ingested food from the mouth to the esophagus. Following ingestion, food is physically modified through a complex set of actions to constitute a shaped bolus of semi-solid or fluid consistency (11, 22, 31), a process that incorporates tethered motions of the tongue, hyoid bone, and jaw (10, 27, 32–34). Once the bolus has been configured, the tongue participates in the creation and optimization of the accommodating cavity by patterned deformation, followed by retrograde propulsion (6). On delivery of the bolus, the pharynx displaces in a superior direction while the laryngeal aperture occludes, producing a cylinder-like flow chamber (5). Propagating pharyngeal contractions then combine with anterior pharyngeal displacement to produce an orderly flow of the bolus from the pharynx, past the occluded airway, and into the esophagus (13, 15, 23).

The tongue consists of a complex three-dimensional (3D) network of skeletal muscle fibers and fiber bundles, involving both intrinsic fibers, i.e., those fibers possessing no direct connection to bony surfaces, and extrinsic fibers, i.e., those fibers possessing connections to bony surfaces (Fig. 1). The intrinsic musculature consists of a core region of orthogonally aligned fibers, contained within a sheath-like tract of longitudinally oriented fibers. The intrinsic fibers are delicately merged with extrinsic muscles that modify shape and position from a superior (palatoglossus), posterior (styloglossus), and inferior direction (genioglossus and hyoglossus). Considering the tongue as a continuous material, we have previously used diffusion-based MRI techniques to characterize both local (intravoxel) (7, 16, 19, 36) and regional (intervoxel) (8, 9) variations in myofiber alignment.

From a mechanical perspective, the tongue is generally considered to be a variation of a muscular hydrostat, an organ whose musculature both creates motion and supplies skeletal support for that motion (18). As such, it capitalizes on its high water content, and hence incompressibility, to modify its form, without change in volume. Accordingly, our approach considers that lingual tissue mechanics can best be conceived as a set of discretely coupled units of compression and expansion, whose behavior is predicted by its underlying fiber organization. We have previously employed tagged magnetization MRI, a method analyzing the deforming patterns of an arbitrarily defined set of intramural elements, to assess lingual strain during swallowing (17) and by these results created a model of lingual deformation based on the presence of several fundamental synergisms (20) involving both the intrinsic and extrinsic muscle fibers. This model suggests, for example, that during bolus propulsion the act of retrograde displacement of the tongue is due to contraction of the extrinsic styloglossus and hyoglossus muscles combined with hydrostatic expansion due to bidirectional contraction of the intrinsic transversus and verticalis muscles. Muscular hydrostats so conceived optimize speed and flexibility during deformation by such synergistic activity while sacrificing force production. By comparison, force production may be maximized in nonhydrostatic systems by large moment arms about a joint supported by a bony skeleton.

To better resolve the 3D resolved mechanical interactions occurring during the propulsive phase of the swallow, we

Address for reprint requests and other correspondence: R. J. Gilbert, Dept. of Mechanical Engineering, Massachusetts Institute of Technology, 77 Massachusetts Ave., Cambridge, MA 02139 (e-mail: rgilbert @ mit.edu).

The costs of publication of this article were defrayed in part by the payment of page charges. The article must therefore be hereby marked "*advertisement*" in accordance with 18 U.S.C. Section 1734 solely to indicate this fact.

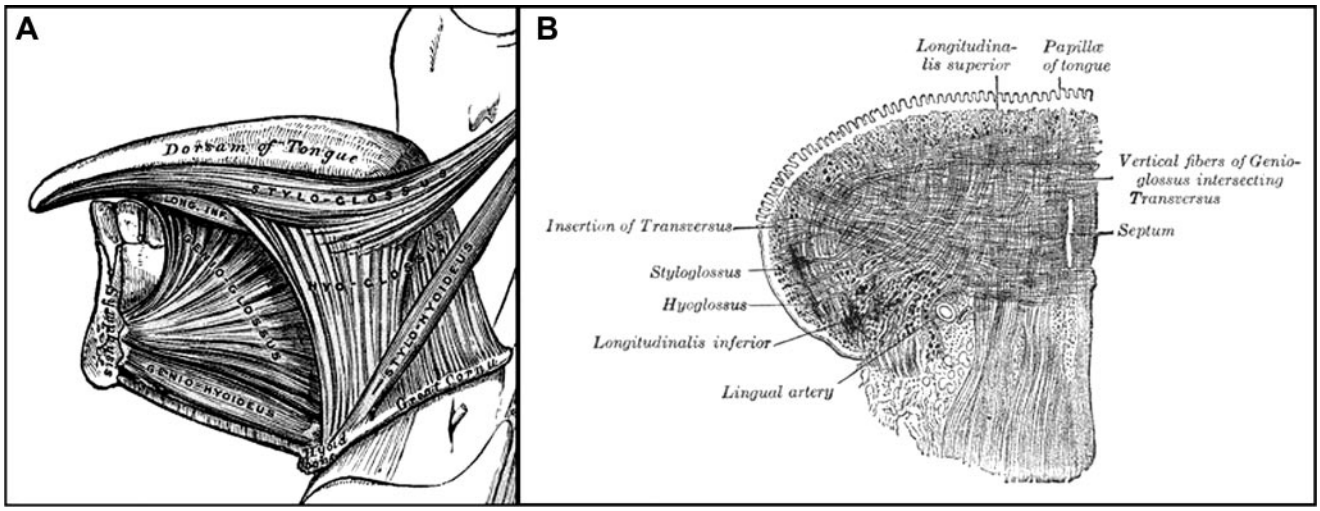

Fig. 1. Anatomy of lingual musculature. Anatomical drawings of the tongue derived from Gray's Anatomy. *A*: midsagittal plane demonstrating complex three-dimensional (3D) network of interwoven skeletal muscle fibers involving the intrinsic muscles (transversus, verticalis, and longitudinalis) and the extrinsic muscles (principally the styloglossus, genioglossus, and hyoglossus). *B*: coronal plane (lateral half) obtained through the mid-portion of the tongue displays the core of transversus and verticalis muscles, surrounded by the styloglossus and hyoglossus (lateral) and the longitudinalis (superior and inferior).

employed gated phase-contrast (PC) MRI to map strain rate tensor arrays (3, 4, 12, 37). This method derives strain rate (directional change of the extent of compression or expansion per unit time by determining the difference between velocity vectors of adjacent voxels distributed throughout the deforming tissue). This approach provides a basis to assay local and regional mechanics during the highly dynamic deformative changes of the tissue and resolves the complete strain rate function for the deforming tongue during the course of liquid bolus propulsion.

METHODS

Subjects ($n = 18$) were chosen for this study who possessed no history or current abnormalities of speech or swallowing. Water bolus (2.5 ml) swallows were performed by the subjects, and MRI was performed in association with each swallow. The timing of image acquisition and retrospective image alignment was gated by lingual pressure applied to the hard palate to visualize the propulsive phase of the swallow. The study was approved by the Massachusetts Institute of Technology Committee on the Use of Humans as Experimental Subjects.

Derivation of local strain rate from PC MRI. Specialized MRI methods exist that derive material motion in tissues from the displacement of MRI-visible patterns (spatial modulations) inscribed on the material's spin distribution. Tagged magnetization employs radiofrequency and gradient pulses to modulate longitudinal magnetization in a manner that results in two-dimensional (2D) bands of saturated magnetization that may be tracked during deformation (17, 18, 20). In contrast, PC MRI determines the local (single voxel) velocity function by applying a phase gradient followed by a canceling (decoding) phase gradient, then deriving local motion by phase shift exhibited by the resulting magnetic resonance images along the gradient vector (3, 24, 37). During PC MRI, velocity encoding is typically applied in four quadrilateral directions (x, y, z; $-x, -y, z$; $x, -y, -z$; $-x, y, -z$) and strain rate determined by the difference in velocities between adjacent voxels distributed throughout the sampled slices of tissue. The strain rate tensor is over specified by taking measurements in four quadrilateral directions, thus canceling out artifacts and other effects on the phase unrelated to velocity. During deformation, strains near each point in the material can be linearly approximated by the strain tensor, given by a 3×3 matrix. There are several advantages to the use of PC methods to assay material strain during rapid physiological motions: *1*) PC MRI provides motion sensitivity that can be set to high values by adjusting the gradient pulse intensities. Thus PC data have near perfect motion specificity and may be analyzed by automated schemas. Combining PC with single-shot image acquisition significantly strengthens the quality, sensitivity, and specificity of PC data by excluding the influence of variable motion across multishot acquisitions that otherwise would be amplified by strain calculation. *2*) In contrast to tagged magnetization, PC MRI provides a basis for the acquisition and analysis of 3D strain. This, however, requires an increase in the number of strain encoding axes and thus requires slightly longer acquisition times (due to reduced sensitivity) and exhibits some algorithmic fragility. Although magnetic susceptibility artifacts resulting in spatial distortions may occur during the course of oral cavity imaging due to the fact that acquisitions must be performed at air-tissue interfaces (25), these effects appear to be relatively small at the edges of the lingual tissue (6) imaged in vivo and are not detectable in the interior of the tissue (17–19) where strain rate measures are performed. Individual PC images were determined to have a signal-to-noise ratio of 48.5.

Strain was calculated by employing an unsupervised and objective algorithm developed in Mathematica. In this paper, all strains are represented as Lagrangian. To determine strain rate per voxel, the difference of phase between voxels at location (i, j) was calculated:

$$\frac{\partial a_{i,j}}{\partial x} = \frac{(a_{i+1,j+1} - a_{i,j+1}) + (a_{i+1,j} - a_{i,j})}{2}$$

$$\frac{\partial a_{i,j}}{\partial y} = \frac{(a_{i+1,j+1} - a_{i+1,j}) + (a_{i,j+1} - a_{i,j})}{2}$$

where $a_{i,j}$ is the phase at voxel (i, j), and x and y are the principal orthogonal directions oriented longitudinally and vertically, respectively. Four voxels were used instead of two so that x-strain tensors and y-strain tensors would be calculated for the same location.

The signal-to-noise ratio was improved by averaging over 10 data sets and weighting the strain rate data by the strength of the magnitude in the following manner:

$$\sum_{k=1}^{10} \mathrm{Min}(m_{i+1,j+1,k}, m_{i,j+1,k}, m_{i+1,j,k}, m_{i,j,k}) \cdot \left(\frac{\partial a_{i,j}}{\partial x}\right)_k = \frac{\partial a_{i,j}}{\partial x}$$

where $m_{i,j}$ is the magnitude at voxel (i,j), and k is the designator for

one of the 10 sets being averaged. Weighted averaging ensured that noise from images with weak signals was removed from the data.

To determine the difference in velocity, the phase difference must be processed with the velocity encoding, VENC. The difference in velocity over the length of the voxels (L) defines the strain rate $\partial\varepsilon/\partial t$.

$$\frac{\partial \varepsilon_{ap}}{\partial t} = \frac{\frac{\partial a}{\partial p} \cdot \mathrm{VENC}}{L}$$

$$\varepsilon_{ap} = \frac{\partial u_a}{\partial p}$$

where p represents any principal vector x, y, or z, and u_a is the material displacement along vector a.

The relation between the four equilateral gradient vectors, a, b, c, and d, and the two principal vectors, x and y, is

$$\frac{\partial \varepsilon_{xp}}{\partial t} = \left(\frac{\partial \varepsilon_{ap}}{\partial t} + \frac{\partial \varepsilon_{bp}}{\partial t} - \frac{\partial \varepsilon_{cp}}{\partial t} - \frac{\partial \varepsilon_{dp}}{\partial t} \right) \frac{\sqrt{3}}{4}$$

$$\frac{\partial \varepsilon_{yp}}{\partial t} = \left(\frac{\partial \varepsilon_{ap}}{\partial t} - \frac{\partial \varepsilon_{bp}}{\partial t} + \frac{\partial \varepsilon_{cp}}{\partial t} - \frac{\partial \varepsilon_{dp}}{\partial t} \right) \frac{\sqrt{3}}{4}$$

The orthogonal dimensions were translated into principal strain vectors with no shear strain. First, rotational strain was removed by separating the symmetric and asymmetric strain tensors, as follows (39):

$$\frac{\partial V_p}{\partial q} = \frac{\partial \varepsilon_{pq}}{\partial t}$$

$$T = \begin{bmatrix} \frac{\partial V_x}{\partial x} & \frac{\partial V_x}{\partial y} \\ \frac{\partial V_y}{\partial x} & \frac{\partial V_y}{\partial y} \end{bmatrix}$$

where V is the local velocity vector field of the material, and p and q represent any principal vectors. The strain rate tensor field (T) can be separated into symmetric (S) and anti-symmetric (A) components:

$$T = S + A = \frac{T + T^T}{2} + \frac{T - T^T}{2}$$

$$S = \begin{bmatrix} \frac{\partial V_x}{\partial x} & \frac{1}{2}\left(\frac{\partial V_x}{\partial y} + \frac{\partial V_y}{\partial x} \right) \\ \frac{1}{2}\left(\frac{\partial V_y}{\partial x} + \frac{\partial V_x}{\partial y} \right) & \frac{\partial V_y}{\partial y} \end{bmatrix} = \frac{1}{2}\left[\nabla V + (\nabla V)^T \right]$$

The symmetric tensor represents stress and strain, whereas the anti-symmetric tensor represents local rigid body rotation. The principal strain vectors were then found using Mohr's circle.

$$\varepsilon_1 - \frac{\varepsilon_x + \varepsilon_y}{2} = \frac{\varepsilon_x - \varepsilon_y}{2} \cos 2\theta + \varepsilon_{xy} \sin 2\theta$$

$$\varepsilon_{12} = -\frac{\varepsilon_x - \varepsilon_y}{2} \sin 2\theta + \varepsilon_{xy} \cos 2\theta$$

To represent the local strain rate tensor for each voxel, the principal strain rates for the tissue contained in each voxel were rendered as 2D icons (Fig. 2). For this study, strain rate was represented graphically using rhombi with their long dimension parallel to a strain rate eigenvector and the length proportional to its magnitude. The width of each rhombus was arbitrarily set proportional to the length for the purpose of visualization. For each voxel, two orthogonally aligned rhombi were generated representing the primary strain rate vector, $\partial\varepsilon_1/\partial t$, defined as that vector with the greatest magnitude, and the secondary strain rate vector, $\partial\varepsilon_2/\partial t$, whose magnitude was smaller and aligned orthogonal to the primary strain rate vector. In the current study, we employed the convention that blue indicates a positive principal strain rate, consistent with expansion, and that red indicates a negative principal strain rate, consistent with compression. It should be noted that compressive and expansive principal strain rates present in a given voxel may or may not be equivalent in magnitude, although the hydrostatic condition requires that their sum be zero if there is no strain in through plane direction. Each rhombus was overlayed in the correct position on the magnitude images of the tongue during the propulsive image sequence.

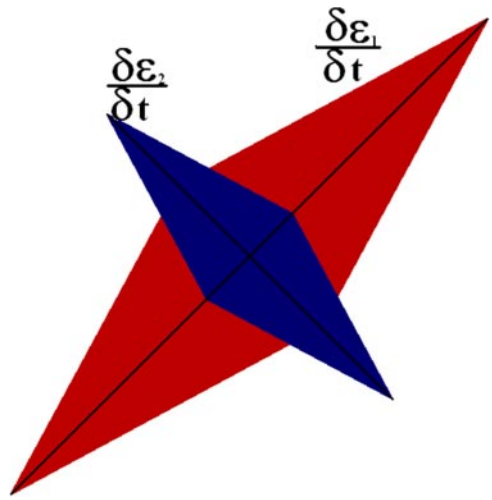

Fig. 2. Icon depicting two-dimensional (2D) strain rate tensor. The orthogonal principal strain rates, reflective of the material strain in each voxel, are displayed in the form of 2 orthogonal rhombi. In each instance, the length and orientation of the larger rhombus is defined by the magnitude and direction of the primary strain rate $\partial\varepsilon_1/\partial t$ (width is arbitrarily displayed proportional to the length for improved visualization). The smaller rhombus is overlaid orthogonal to the larger rhombus and possesses length and orientation defined by the secondary strain rate $\partial\varepsilon_2/\partial t$. By convention, if a rhombus is blue, the strain rate represented is positive (expansion), and if a rhombus is red, the strain rate is negative (compression). In the example shown in this figure, the primary strain rate tensor is compressive and represented as a red rhombus, whereas the secondary strain rate tensor is expansive and represented as a blue rhombus possessing a magnitude of 60% as large as the primary strain rate tensor.

Although each voxel constitutes a unique strain rate tensor, mechanical analysis of mean deformation of voxel arrays was also performed. This approach provides adequate signal to noise to allow quantitative comparisons to be made between subjects as a function of location and temporal position in the swallow. Regions of the tongue were delineated from sagittal PC images and comparisons made of mean magnitude of compressive and expansive strain rates. The regions consisted of the following: *region 1*, superior-posterior tongue, comprising the distributions of the posterior genioglossus, verticalis, and transversus muscles, and points of insertion for the styloglossus and hyoglossus; *region 2*, superior-middle tongue, comprising the middle genioglossus, verticalis, and transversus muscles; *region 3*, superior- anterior tongue, comprising the anterior genioglossus and verticalis and transversus muscles; and *region 4*, inferior-middle tongue, comprising largely the distributions of the inferior genioglossus and hyoglossus muscles. The image sizes defined by *regions 1*, *2*, and *3* were ~100 voxels, whereas the image size defined by *region 4* was ~50 voxels. The explicit boundaries of these regions were arbitrarily defined, acknowledging the continuous nature of lingual fiber myoarchitecture. Comparisons were made of the mean ± SD of strain rate amplitude between regions within each time point of duration 54 ms (0, 200, 400, and 600 ms following application of the lingual trigger) and between time points for a single region. Statistical comparisons were obtained employing the Student's t-test, with significance assigned at $P < 0.05$.

Validation of PC MRI for deriving local tissue strain rate. To validate the method for deriving local strain rate from PC MRI, we tested the current MRI pulse sequence and method of analysis during deformation induced by a synchronized mechanical plunger apparatus (24) in a phantom gelatinous material (4% Agar). This system assays local compression and expansion in the phantom following forced compression of the material by the plunger at varying rates of displacement. Similar to the case of the tongue, the gel density is constant, i.e., the material is incompressible, and thus the trace of the strain tensor must always be zero. However, the gelatinous material is different from the tongue since it is a purely isotropic material, and thus all local compression will be balanced by expansion in the case of each voxel. The deformation of a hydrostatic muscle, such as the tongue, is controlled by local anisotropic elements, i.e., muscle fibers and fiber arrays, which by their combined contraction and relaxation produce local compression and expansion. Nonetheless, this method provides a way to verify the basic tenets by which local phase shifts are translated into material properties, i.e., local compression and expansion. The experiment was run on a 1.5-T Siemens Avanto magnet with an echo time of 80 ms, a repetition time of 650 ms, and VENC of 0.2 cm/s. Voxels were $5 \times 5 \times 5$ cm^3. The plunger apparatus has a sinusoidal period of 750 ms and a stroke length of 0.6 cm. The motor sends a 5-V trigger impulse to a single arbitrary point during its cycle. Single acquisitions are taken in 25-ms intervals for a total of 30 strain rate images. The data in Fig. 3 display the localized strain rate of the gel at three times during the plunger's cycle. When the plunger is not in contact with the gel, no significant strain rate patterns are measured. This is consistent with the assumptions of a static system. The line of vertical compression on the right side of the plunger is probably due to edge effects between the gel and the air. During the downward-moving portion of the cycle, a consistent strain pattern of vertically oriented compression underneath the plunger occurs, along with orthogonal expansion due to the isovolemic properties of the gel. During the upward-moving portion, an equal but opposite pattern of vertically oriented expansion occurs under the plunger, accompanied by orthogonal compression. These observations substantiate that the strain rate derived from PC MRI, as defined above, is representative of the local compressive and expansive events associated with local material deformation.

Physiological gating of MRI. Given the spatial and temporal complexity of the mechanical events associated with swallowing and the one-dimensional nature of conventional PC data, gating is needed to temporally align the resulting mechanical information. Although superior temporal precision would result from cine magnetic resonance (MR) image acquisition (29), obtaining multiple PC MR images following a single gating pulse was not feasible. Owing to the fact that propulsion is principally reflexive once initiated, we elected to tether MR image acquisition to lingual pressure applied to the hard palate

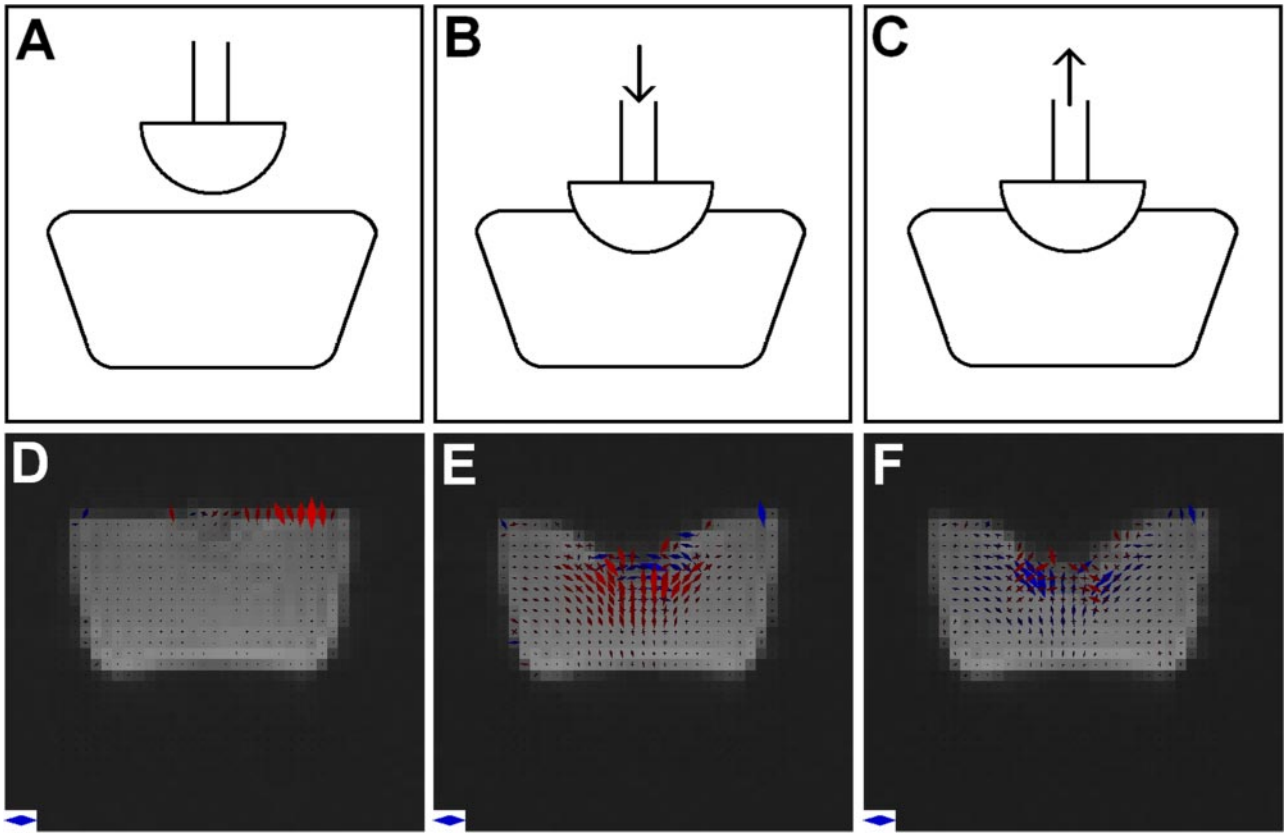

Fig. 3. Validation of PC MRI as a method to derive local strain rate. To validate the method by which local strain rate tensors are derived from PC MRI, we employed a mechanical plunger apparatus to induce compressive or expansive deformation in a gelatinous phantom material. The plunger consists of hemispherical plastic device whose position is controlled by a stepper motor, which can be lowered or raised relative to the gel at a rate of 1 Hz and a stroke length of 1.2 cm. Strain rate was derived from local PC as described in METHODS, and the resulting primary and secondary strain rate tensors are depicted as rhomboid icons for each voxel. The diagrams displayed in the *top* row depict the plunger's position relative to the gel before contact (*A*), during a downward stroke (compression) (*B*), and during an upward stroke (expansion) (*C*). The images displayed in the *bottom* row depict the strain rate vectors within the gel before contact (*D*), during the downward stroke (*E*), and during the upward stroke (*F*). A consistent field of vertical compression can be seen below the plunger during the downward stroke, accompanied by orthogonal expansion due to the gel's isovolemic nature. An analogous field of vertical expansion can be seen below the plunger during the upward stroke, accompanied by orthogonal compression. The strain rate icon displayed for scale in the *bottom left* of each image represents 0.20 s^{-1}.

through a pressure-sending bulb at the approximate outset of the propulsive phase (21, 28). The device configuration is portrayed in Fig. 4. A small (3-cm length) tongue bulb [Iowa Oral Performance Instrument (14), Blaise Medical] was placed immediately behind the front teeth and on the tip of the subject's tongue. The bulb was connected via 15 m of 1/16-in. ID tubing to a pressure sensor, from which output was acquired and analyzed by Labview software. The peak pressure occurring secondary to tongue pressure against the bulb was recorded, and a 5-V output signal was triggered when a threshold pressure (~0.35 PSI) was achieved. Acknowledging that there is likely to be variation between subjects in the pressure applied by the tongue during swallow initiation, the exact pressure threshold was derived for each subject by determining the voltage threshold immediately preceding the swallow in four to eight test swallows, then setting the voltage threshold to 0.01 V below the smallest peak achieved in the test swallows. Although the interval between the time of initial tongue contact with the sensor and the achievement of threshold pressure varied slightly between subjects, the interval between the time at which threshold pressure was obtained and the initiation of lingual displacement (and the coordinated initiation of MR scanning) was <0.1 s and highly reproducible. It is conceivable that the presence of the bulb in the oral cavity may cause a deviation from the natural positioning of the tongue and thus induce compensatory mechanical actions. In addition, the resistance provided by the bulb may modify the natural strain patterns exhibited by the tissue during the course of swallowing. Although in preliminary experiments the bulb was easily positioned by subjects by placing one edge of the bulb against the teeth, resulting in tongue-tip displacement, there was a small amount of accommodative lingual deformation and superior hyoid displacement as a function of bulb positioning in the anterior oral cavity (Fig. 4*C*). The effect of this preswallow accommodative effect could not be systematically assessed in the current protocol since the presence of the intra-oral device was essential to the acquisition of MR data.

MRI data acquisition. Each subject swallowed 2.5 ml of water four times to compile a complete set of strain data at one time interval in two slices. The water was delivered via a subject-controlled syringe attached to rubber tubing that inserted into the side of the subject's mouth. Ten sets of strain data were then averaged together in each image, and four different time intervals were sampled, resulting in a total of 160 swallows per subject to create complete data set of four time intervals and two adjacent slices. We also point out that our method incorporates an internal control for subject fatigue, that is, the magnitude of the pressure applied to the intra-oral bulb during the course of the swallow. Interestingly, by this measure, our subjects did not demonstrate any evidence of fatigue during the course of these trials. In these experiments, the volume observed was comprised by two slices; each is made up of a set of $3 \times 3 \times 3$ mm^3 voxels located adjacent to and on the left and right of the midsagittal plane. The application of each velocity encoding pulse was elicited by a 5-V electrical signal triggered by tongue pressure on the hard palate. Acquisitions occurred at 0, 200, 400, and 600 ms from the elicitation of the trigger point. The pulse sequence is similar to the one used by Tseng et al. (35). Specific imaging parameters included echo time of 54 ms, repetition time of 274 ms, and VENC of 0.67 cm·s^{-1}·cycle^{-1}. One acquisition was performed in each slice per swallow, and acquisitions alternated between the two slices. The effective repetition time for a particular slice was never <3 s and determined by the speed at which the subject could comfortably swallow repeatedly. The technique was validated over 13 subjects, whereas quantitative gated PC data was obtained in 5 subjects (3 men, 2 women). Data was acquired using a 1.5-T Siemens Avanto whole body scanner equipped with two custom-built surface coils, ~150 mm^2 in area, placed on each cheek and gently secured with tape.

RESULTS

Experiments were performed to assess the local strain rate function occurring in the tongue musculature during the propulsive phase of swallowing. Strain rate was derived from the phase differences recorded within temporally sequenced MR images, and the resulting strain rate tensors superimposed in the form of quantifiable icons on the magnitude images of the tongue during deformation. Inasmuch as strain rate values are provided in Lagrangian terms, they have units of s^{-1}. Thus zero defines an absence of strain, whereas a strain rate that would increase the length of the material by 100% per second may be represented as 1 s^{-1}. We demonstrate in Fig. 5 the prototypical bulk motion of the tongue during the propulsive phase of a 2.5-ml water bolus swallow. The image sequence shown depicts the magnitude images acquired during a period

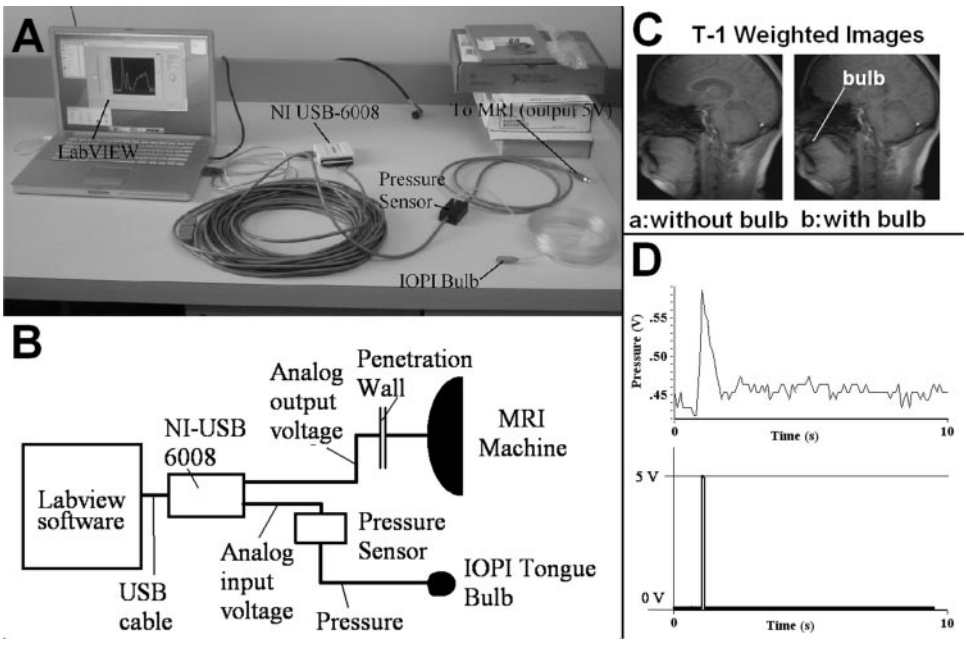

Fig. 4. Mechanism for gating PC MR image acquisition. A swallow-based MR acquisition gating system was developed to provide a basis for precise temporal sequencing and spatial registration based on the pressure applied by the tongue to a sensing bulb (Blaise Medical) situated against the hard palate at the outset of late accommodation. On achieving threshold pressure, a 5-V signal is elicited, which triggers MR acquisition. *A*: photograph of system components, consisting of a small (3-cm length) tongue bulb in series via 1/16-in. ID tubing with a pressure transducer whose output is directed to Labview hardware/software and a pressure driven 5-V trigger signal elicited. *B*: block diagram of system components. *C*: magnitude MR images of the tongue in the absence of (a) and the presence of the gating bulb (b), indicating accommodative lingual deformation and hyoid displacement as a function of bulb position. *D*: pressure tracing (*top*) induced by the tongue applied to the hard palate via the sensing bulb and the threshold for eliciting an electrical trigger pulse (*bottom*).

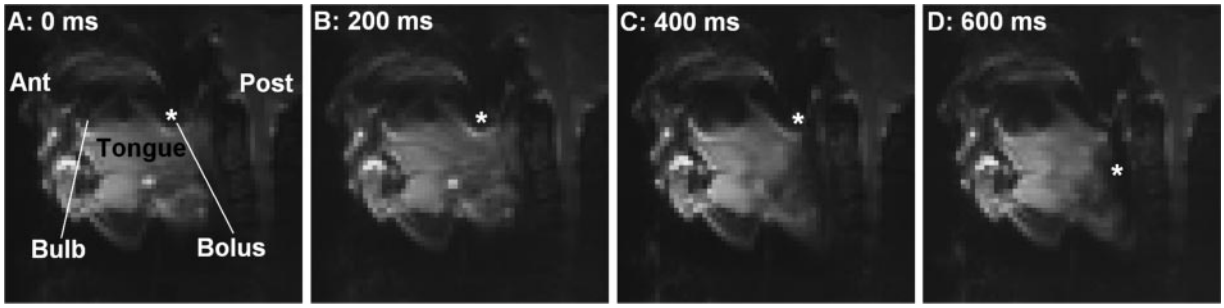

Fig. 5. Demonstration of lingual pattern of deformation during bolus propulsion. Sequence of magnitude MR images intended to demonstrate the characteristic pattern of lingual deformation associated with propulsion of the liquid bolus from the oral cavity to the pharynx. Eighty magnitude images were acquired per time point and averaged together to create an image of the tongue at four time points during swallowing: 0, 200, 400, and 600 ms following trigger pulse application. The pocket of low signal located in the anterior-superior oral cavity is the tongue bulb employed for recording lingual pressure applied to the hard palate, whereas the pocket of low signal in the posterior-superior oral cavity represents the approximate position of the liquid bolus (shown with an asterisk in each image).

of time sufficient to complete the propulsive action (generally 600 ms). The images display the averaged intensity of the complete set of magnitude images at each time point for a representative subject, with brightness proportional to signal intensity. The position of the pressure-sensing bulb is shown as a signal void in the anterior oral cavity, whereas the approximate position of the water bolus is detected as a signal void in the posterior oral cavity. An example of raw magnitude and phase data for a single time point (0 ms in the image sequence shown in Fig. 5) is displayed in Fig. 6. In the top row are shown the four individual magnitude images taken with the four encoding gradients (at the same spatial resolution as the phase images below). The bottom row displays the corresponding phase images, with white representing a phase shift of $+180°$ and black representing a phase shift of $-180°$. The shading gradient is proportional to the change in strain in the direction of the phase gradient. The tongue exhibits varying levels of phase contrast, consistent with varying strain rates, whereas the relatively small gradient within the brain indicates minimal to no strain rate. The snowy pattern around the head is indicative of random phase data and is consistent with a low signal area. It should be noted that the region of the middle tongue in which black borders on white does not indicate a steep phase gradient but suggests that the phase has "rolled over" from $+180°$ to $-180°$, a condition assumed by the strain rate algorithm to possess the smallest possible phase difference.

The strain rate tensors were calculated from the PC data and overlayed on the magnitude images as icons during a 2.5-ml water bolus swallow. We display in Fig. 7 (single subject) and Fig. 8 (all sagittal subjects combined) the strain rate sequence at 0, 200, 400, and 600 ms following the application of the gating pulse. The data at each time point was measured in 54 ms, but acquisitions were limited to four time points and 200-ms resolution to allow sufficient averaging without overexerting the subject. We employ throughout a convention of blue icons representing expansive strain and red icons representing compressive strain (see METHODS), with the orientation of each strain rate icon aligned with the primary and secondary

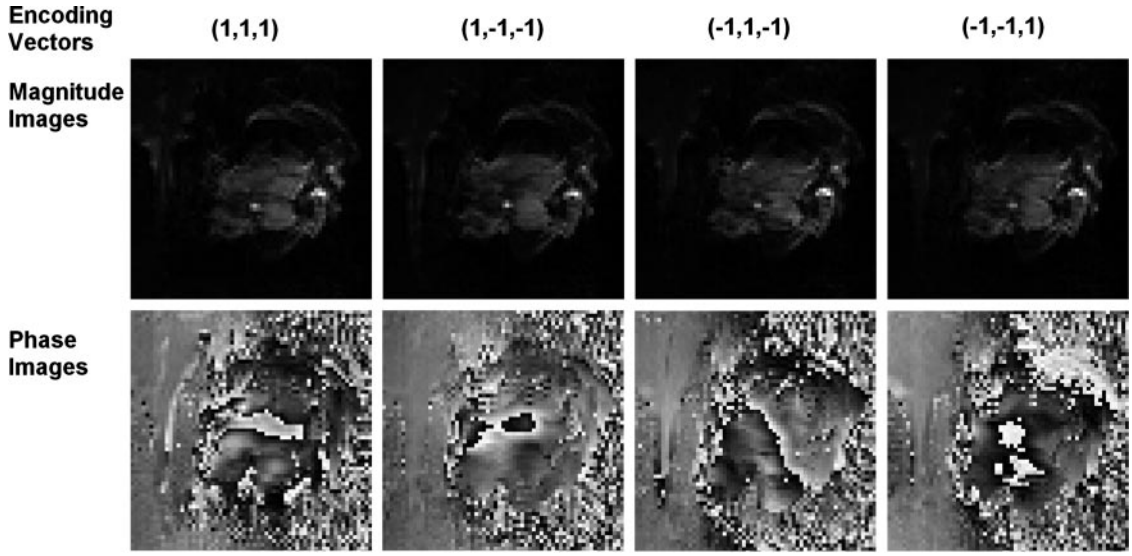

Fig. 6. Raw phase data for generating a single set of unaveraged strain rate tensors. Shown are a set of 4 magnitude (*top*) and associated 4 phase images (*bottom*) specific for each gradient direction in the case of a single time point (0 ms, trigger point). Each strain rate tensor image requires four scans, encoded with four different gradient vectors, embodying a magnitude image and a phase image. The four one-dimensional strain rate arrays are combined into one two-dimensional strain-rate array. Note the contrast between the high strain phase images of the tongue, characterized by gradual shade gradients, the low strain phase images of the brain, characterized by little or no shade gradients, and the low signal areas outside of the head, characterized by the random, snowy phase.

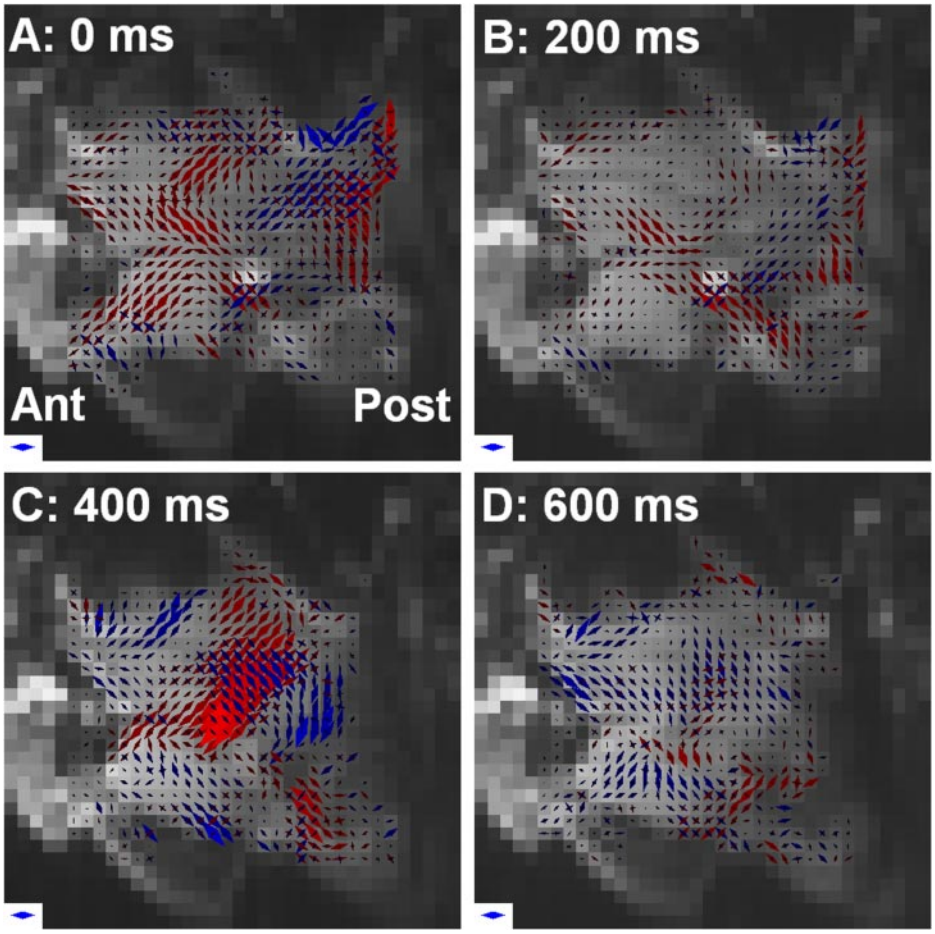

Fig. 7. Strain rate patterns exhibited by the tongue during bolus propulsion (sagittal). Strain rate tensors were derived in a sagittal image slice using PC MRI for a set of voxels comprising the tongue during the propulsive phase of swallowing of a 2.5-ml water bolus. Each image was compiled by averaging two slices, comprising 10 sets of strain rate data each, acquired from 80 swallows total. Principal strain rates within each voxel are shown graphically as rhombi with a long axis parallel to the principal strain vector and length proportional to the magnitude of the strain rate. For each voxel, 2 orthogonally aligned rhombi may be represented for the primary and secondary strain rate. Shown in this figure is a sequence of 4 images obtained from a single subject at 0 (*A*), 200 (*B*), 400 (*C*), and 600 ms (*D*) from the application of the gating pulse. The strain rate icon displayed for scale at *bottom left* of each image represents 0.33 s^{-1}.

strain rate vectors and the length of each strain rate icon proportional to the magnitude. This approach allows us to quantify strain rate per voxel and for designated voxel arrays. Acknowledging the continuous nature of the tongue musculature, individual strain rate icons are displayed, although the association of the icons with the distribution of known muscles, i.e., genioglossus, styloglossus, etc., is also noted when appropriate.

The pattern of strain rates occurring during lingual propulsion exhibited a combination of compressive and orthogonally commensurate expansive events distributed throughout the tissue. At the point of gating pulse elicitation, there were four prominent strain rates observed. *1*) Compressive strain (maximum measured compression was 0.33 s^{-1}) was aligned obliquely between the anterior-inferior and the posterior-superior regions of the tongue, with commensurate expansion in the same orientation limited to the posterior-superior region of tissue. These strain rate vectors were coincidental with the alignment of the anterior and posterior distributions of the genioglossus muscle. *2*) Compressive strain (maximum measured compression was 0.40 s^{-1}) was aligned obliquely between the anterior-superior to the posterior-inferior regions (exactly orthogonal to the above noted compressive strains), with commensurate expansion in the posterior superior region of the lingual tissue. *3*) Vertically aligned compressive strain (maximum measured compression was 0.45 s^{-1}) was located in the approximate distribution of the palatoglossus and orthogonal to the surface of the bolus, combined with expansive strain (maximum measured expansion was 0.45 s^{-1}) tangent to the bolus. These latter effects are likely to represent commensurate expansion orthogonal to the palatoglossus and passive effects of the bolus itself. The net effect of these events is the containment and positioning of the bolus in the posterior oral cavity. *4*) Compressive strain (maximum measured compression was 0.36 s^{-1}) was in the posterior-inferior region of the tissue directed obliquely to the styloid process, which is likely to represent passive compression due to contraction of the contractions of the laterally inserted styloglossus. At 200 ms, there were considerably more modest amounts of compressive (maximum measured compression was 0.41 s^{-1}) strain aligned obliquely between the anterior-superior and the posterior-inferior regions of the tissue, with commensurate orthogonal expansion (maximum measured expansion was 0.30 s^{-1}) in the posterior region, along with vertically and obliquely aligned compressive strain (maximum measured compression was 0.29 s^{-1}) in the posterior-superior tissue. At 400 ms, there was prominent compressive strain (maximum measured compression was 0.63 s^{-1}) occurring in the middle and posterior tissue regions and aligned obliquely between the anterior-inferior and the posterior-superior regions of the tongue (consistent with contraction of the genioglossus and styloglossus) with commensurate orthogonal expansion (maximum measured expansion was 0.38 s^{-1}) and vertically aligned expansion (maximum measured expansion was 0.48 s^{-1}). At 600 ms, there was

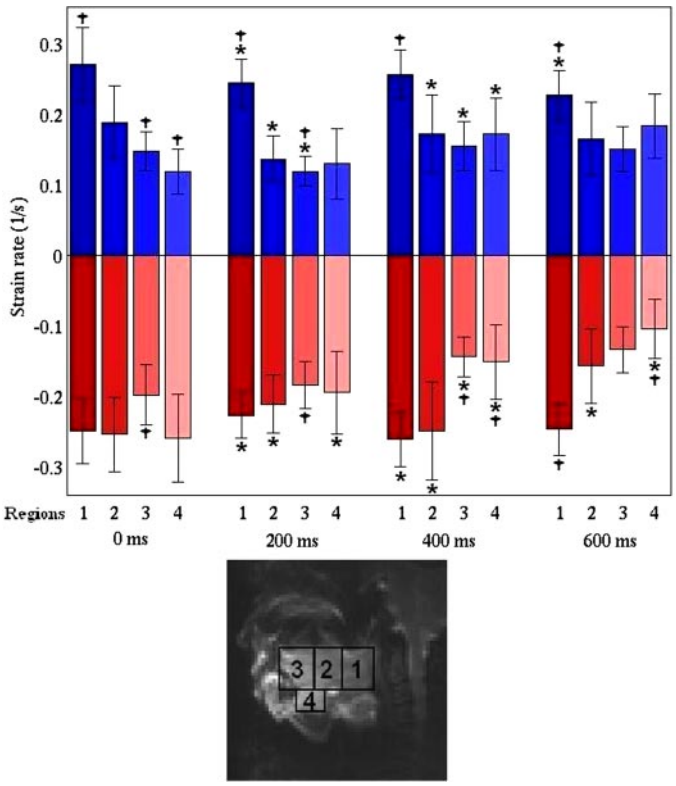

Fig. 8. Combined lingual mechanical data (sagittal). The mean expansion (blue) and compression (red) for 3 subjects, comprising 30 acquisitions total, in the *x* and *y* directions (sagittal orientation) in four different regions of the tongue were graphed separately, as displayed in the reference image. The regions consisted of the *1*) superior-posterior, *2*) superior-middle, *3*) superior-anterior, and *4)* inferior-middle and were empirically selected based on patterns of strain rate observed. Comparisons were made of the mean ± SD of strain rate amplitude between regions at a single time point which was 0, 200, 400, and 600 ms following application of the lingual trigger pulse (displayed as †) and between different time point for a single region (displayed as *).

expansive strain aligned in three identifiable orientations (maximum measured expansion was 0.38 s^{-1}): obliquely between the anterior-inferior and the posterior-superior regions, obliquely between the anterior-superior and posterior-inferior regions, and vertically in the mid and posterior regions of the tissue.

To resolve the mechanical events associated with transverse directed strain, we acquired two coronal images (anterior and posterior tongue) at 0 and 400 ms following the gating pulse (Fig. 9). The exact location of the slice in each instance is shown in the magnitude images (*inset*). In general, the strain events showed sagittal symmetry and a predominance of strain (compressive and expansive) in the posterior tongue at the 400-ms time point. At this time point, in the anterior tongue image, the following was observed: *1*) prominent mid-line compressive strain (maximum strain rate 0.29 s^{-1}) in the inferior portion of the tissue along with commensurate expansion in the superior portion of the tissue, and *2*) oblique and transverse compression (maximum strain rate 0.39 s^{-1}) consistent with bi-directional contraction of the core intrinsic muscles and commensurate orthogonal tissue expansion. At this same time point, in the posterior tongue, the following was observed: *1*) obliquely aligned compressive strain in the lateral and inferior portion of the tissue (maximum strain rate 0.23 s^{-1}), consistent with contraction of the hyoglossus, and *2*) oblique, vertical, and transversely aligned compression in the middle and superior portions of the tissue (maximum strain rate 0.24 s^{-1}) with orthogonal expansion, consistent with contraction of the transversus and verticalis fibers.

DISCUSSION

The tongue is a structurally complex muscular organ that is responsible for the manipulation and transport of food in the oral cavity during swallowing. Through a series of precisely timed shape changes, the tongue first configures and then propels the ingested bolus of food from the oral cavity to the pharynx. Conceiving the basis for lingual deformation during swallowing requires an understanding of how the organ moves in relation to extrinsic structures, such as the jaw and hyoid bone, as well as the underlying relationship between intramural structure and function. To conceptualize the vast array of mechanical operations associated with lingual deformation, we have considered the tongue as a muscular hydrostat, a muscular structure defined by its ability both to create motion (via tissue displacement) and provide the skeletal support for that motion (via elongation and stiffening) (27, 28). The mammalian tongue is a particularly interesting form of hydrostat since its deformations are predicated on the contractions of both intrinsic and extrinsic muscle fibers merged structurally and functionally within the body of the tongue. The designation of the tongue as a muscular hydrostat infers several important properties, namely the coexistence of orthogonally aligned muscle fiber populations, which contract synergistically to generate physiological motion and the conceptualization of the tissue as an array of contiguous elements producing varying degrees of compressive or expansive strain.

We have previously studied lingual mechanics during prototypical deformations, i.e., protrusion and bending, and during swallowing with tagged magnetization MRI (17, 18). This method quantifies local strain by tracking the deformation of a 2D grid of saturated magnetic bands superimposed on the MR image. By this approach, we assayed the lingual musculature during each of the cardinal phases of the swallow, namely early accommodation (bolus held in the anterior oral cavity), late accommodation (bolus transferred to the posterior oral cavity), and propulsion (bolus propelled retrograde from the oral cavity to the pharynx). These experiments, combined with the results of our previous work (6, 15), allowed us to consider several postulates regarding lingual deformation during the swallow: *1*) the containment of the bolus during early accommodation results from a synergistic contraction of the anterior genioglossus, combined with the contractions of the hyoglossus, verticalis, and transversus muscles; *2*) the posterior shifting of the bolus during late accommodation results from an increase in inferior directed strain located in the posterior tongue and is related principally to contractions of the hyoglossus and genioglossus muscles; and *3*) the prototypical deformation of the tongue occurring during propulsion results from the effects of posterior directed contraction of the styloglossus and possibly bidirectional contraction of the transversus and verticalis muscles (30). It should be noted that contraction of the styloglossus alone could not generate expansive strain above its insertion point in the mid-portion of the tongue's lateral surfaces since the tongue is constrained from below.

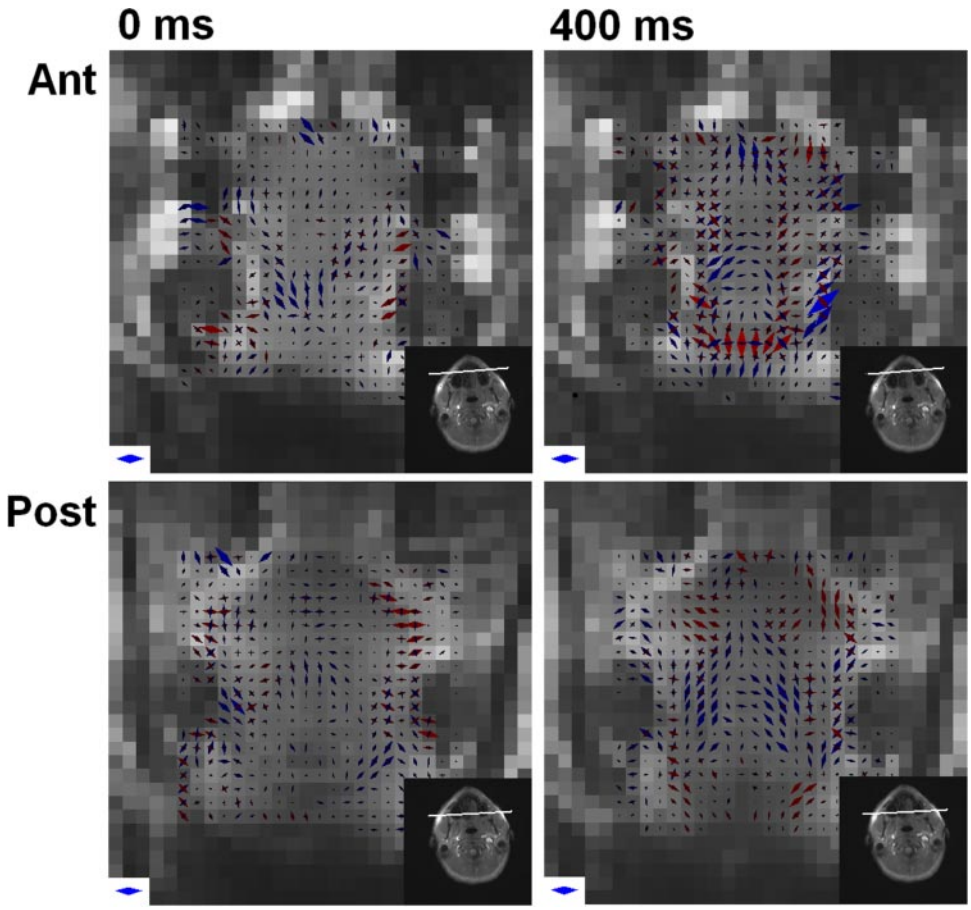

Fig. 9. Strain rate patterns exhibited by the tongue during bolus propulsion (coronal). Strain rate tensors from a single subject were derived by PC MRI during a 2.5-ml water bolus swallow and displayed at 0 and 400 ms in 2 coronal image slices from the anterior and posterior tongue. Each image was compiled by averaging two slices, comprising 10 sets of strain rate data each, acquired from 80 swallows total. *Top*: midsagittal image slice. *Middle*: anterior coronal slice. *Bottom*: posterior coronal slice. The slice location for each strain tensor images is shown at *left*. These results demonstrate that the early posterior directed compressive strains (0–200 ms) are followed at 400 ms by compressive strains directed along the direction of the tranversus and the vertically aligned genioglossus and verticalis fibers. The latter mechanical events possess close temporal correlation with the major component of retrograde expansion characteristic of the propulsive phase. The strain rate icon displayed for scale in the *bottom left* of each image represents 0.33 s^{-1}.

These results illustrate an important limitation in the use of tagged magnetization in the study of lingual mechanics, namely the inability to resolve spatially complex and dynamic 3D strain fields. To address this issue, we modified a technique previously applied to the study of cardiac mechanics, gated PC MRI (3, 4, 12, 37), to characterize lingual mechanical function. From a practical perspective, velocity encoding is applied in four directions and strain rate derived from the difference in velocity between adjacent voxels for each gradient direction. This latter requirement, in combination with the relatively low MR signal intensity resulting from velocity encoding, provides the rationale for image gating to achieve temporal reconstruction. In contrast to prior approaches for temporal reconstruction of the swallow employing superficial EMG recordings (23), we employed in this study a novel method to gate MR acquisition based on the signal resulting from peak lingual tip pressure applied to the hard palate through an intra-oral pressure-sensing bulb during early propulsion. We demonstrated in preliminary studies that the interval between the achievement of threshold lingual pressure and the initiation of the propulsive deformation is quite short ($<$0.1 s) and highly reproducible. This form of MR gating provides both timed MR acquisitions as well as a method for accurate retrospective sequencing of the images acquired. It should be acknowledged however, that lingual pressure-gated swallows may differ from physiological swallows due to the presence of the bulb in the anterior oral cavity and the effects of the bulb on preswallow lingual mechanics. These effects include a small, but significant, effect on lingual shape and superior hyoid displacement, which may itself be accentuated by the fact that subjects were required to maintain a supine position in the MRI scanner apparatus. Although important, these effects were largely mitigated by the facts that the pressure exerted by the bulb on the surface of the tongue was negligible, as indicated by the relatively small amount of air displaced from the bulb relative to the air within the tubing, and the space occupied by the bulb was largely eliminated by the pressure applied by the tongue to the hard palate through the intra-oral bulb. Lastly, our previous studies have demonstrated the capacity of subjects to swallow repeatedly in this position. Thus, although effects of bulb presence and subject position on swallow mechanics are unavoidable, these effects should be relatively small during the active phases of deformation.

Through the application of gated PC MRI, we studied the mechanisms involved in the genesis of rapid lingual reconfiguration during propulsion. Our current results demonstrate that the propulsive phase of swallowing is associated with a tightly organized series of compressive and expansive events occurring within a period of ~600 ms. In the initial portion of the propulsive phase (images obtained at the time of gating pulse application and 200 ms from the gating pulse), we observed the following events: *1*) obliquely aligned compressive and expansive strain in the approximate fan-like distribution of the genioglossus, *2*) vertically aligned compressive strain consistent with passive compression secondary to palatoglossus contraction and active compression secondary to verticalis con-

tractions combined with orthogonal expansion, *3*) compressive strain aligned obliquely between the anterior-superior to the posterior-inferior regions with commensurate expansion in the posterior superior region, effects possibly related to passive compression due to laterally inserted contraction of the hyoglossus, and *4*) compressive strain aligned obliquely and directed to the styloid process. The latter may reflect passive compression due to the laterally inserted fibers of the styloglossus or active compression secondary to more medially inserted fibers. The combined effect of these mechanical events is the effective reconfiguration of the tongue before posterior displacement. Lingual deformation during the latter portion of the propulsive phase (images obtained at 400 and 600 ms from the gating pulse) appeared to involve prominent compressive strain occurring in the mid and posterior region of the tissue obliquely aligned between the anterior-inferior and posterior-superior regions of the tissue, suggestive as well of the distribution of the genioglossus with commensurate orthogonal expansion, along with bidirectional contraction in the approximate distribution of the intrinsic core fibers and expansion in the anterior-posterior orientation. Interestingly, this expansive phase coincided precisely with the delivery of the flattening of bolus-containing concavity and the apparent delivery of the bolus to the pharynx. Despite some intersubject variation in the precise timing of compressive and expansive strain rates, these general patterns were exhibited by all subjects, thus substantiating the postulate that the cardinal lingual motions are a due to mechanical interactions of the intrinsic and extrinsic muscles.

This approach constitutes a significant advance over previous techniques since it provides a method to assay simultaneously the rates of compression and expansion during physiological motion. This technique may potentially be combined with measures of underlying lingual myoarchitecture, thus constituting a method by which the rate and direction of fiber shortening can be determined. We previously considered the proposition that propulsive lingual deformation is associated with a combination of internal stiffening and hydrostatic elongation resulting from the bidirectional contraction of the transversus and verticalis muscles combined with retracting force applied by the laterally inserted styloglossus (17). We have now extended this conceptualization of tongue deformation to include a more complex sequence of material strains (compression and expansion) involving the various segments of the genioglossus muscle, tight integration of extrinsic and intrinsic strain behavior, and passive elements of compressive and expansive strain related to contractions not included in the particular imaging slice, i.e., styloglossus and hyoglossus, and secondary mechanical events imposed by the tongue's inherently isovolemic conditions. It should be recognized that the exact timing of the events described may vary somewhat with prior descriptions of lingual deformation due to the presence of the bulb in the oral cavity and changes in lingual shape and mechanics before the initiation of the observed sequence.

The extension of PC MRI, previously applied to determine cardiac strain, to imaging the mechanical function of the tongue during swallowing contained several technical challenges, owing to the fact that the tongue is both structurally and mechanically more complex than the heart. By establishing a method of MRI gating associated with threshold lingual pressure applied to the hard palate during late accommodation and by adopting a velocity encoding for the highly variable strain rates exhibited by the tongue with minimal artifact attributable to the air-tissue interface in the oral cavity, we were able to achieve reliable strain rates involving the tongue during swallowing. However, several limitations of this approach should be acknowledged. Although generally consistent mechanical patterns were exhibited, some of the events shown were quite variable. By our analysis of this variability, it may be that precise time where certain mechanical events occurred varied subtly but significantly between subjects, an issue that could become even more important in the case of pathological tongue motion. We anticipate accordingly that future studies may thus require considerably greater temporal resolution. A second limitation was the need to resolve transverse planar strain separate from anterior-posterior planar strain. Although the high degree of mechanical symmetry and coherent strain rate patterns exhibited by the tongue indicate that we are accurately measuring strain rate in the tongue, there are theoretical limitations for resolving complex intravoxel strain patterns that would be helped through the use of techniques capable of acquiring 3D strain rate directly. We should also acknowledge that, since our current approach is directed to resolving internal tissue strains, it does not have sufficient resolution to accurately determine surface deformation or possess appropriate contrast to visualize bolus displacement (1, 2, 23, 38). Thus the relationship between internal strain and physiological bolus manipulation cannot be measured directly with the current techniques.

We conclude that gated PC MRI can be adapted with appropriate gating to assay the tongue's internal strain events associated with bolus propulsion. Our results demonstrate that bolus propulsion may be attributed to a synergistic sequence of compressive and expansive mechanical events involving both the intrinsic and extrinsic muscles, whose net effect is the orderly delivery of the ingested bolus from the oral cavity to the pharynx.

REFERENCES

1. **Bardan E, Kern M, Arndorfer RC, Hofmann C, Shaker R.** Effect of aging on bolus kinematics during the pharyngeal phase of swallowing. *Am J Physiol Gastrointest Liver Physiol* 290: G458–G465, 2006.
2. **Chi-Fishman G.** Quantitative lingual, pharyngeal and laryngeal ultrasonography in swallowing research: a technical review. *Clin Linguist Phon* 19: 589–604, 2005.
3. **Dou J, Tseng WY, Reese TG, Wedeen VJ.** Combined diffusion and strain MRI reveals structure and function of human myocardial laminar sheets in vivo. *Magn Reson Med* 50: 107–113, 2003.
4. **Ebbers T, Wigstrom L, Bolger AF, Wranne B, Karlsson M.** Noninvasive measurement of time-varying three-dimensional relative pressure fields within the human heart. *J Biomech Eng* 124: 288–293, 2002.
5. **Flaherty RF, Seltzer S, Campbell TA, Weisskoff RM.** Dynamic magnetic resonance imaging of vocal cord closure during deglutition. *Gastroenterology* 109: 843–849, 1995.
6. **Gilbert RJ, Daftary S, Campbell TA, Weisskoff.** Patterns of lingual tissue deformation associated with bolus containment and propulsion during deglutition as determined by echo-planar MRI. *J MRI* 8: 554–560, 1998.
7. **Gilbert RJ, Daftary S, Reese TG, Weisskoff RM, Wedeen VJ.** Determination of lingual myoarchitecture in whole tissue by NMR imaging of anisotropic water diffusion. *Am J Physiol Gastrointest Liver Physiol* 275: G363–G369, 1998.
8. **Gilbert RJ, Magnusson LH, Napadow VJ, Benner T, Wang R, Wedeen VJ.** Mapping complex myoarchitecture in the bovine tongue with diffusion spectrum magnetic resonance imaging. *Biophys J* 91: 1014–1022, 2006.

9. **Gilbert RJ, Wedeen VJ, Magnusson LH, Benner T, Wang R, Dai G, Napadow VJ, Roche KK.** Three dimensional myoarchitecture of the bovine tongue demonstrated by diffusion spectrum magnetic resonance imaging with tractography. *Anat Rec* 288: 1173–1182, 2006.
10. **Herrel A, Cleuren J, Vree F.** Kinematics of feeding in the lizard Agama stellio. *J Exp Biol* 199: 1727–1742, 1996.
11. **Hiiemae KM, Palmer JB.** Food transport and bolus formation during complete feeding sequences on foods of different initial consistency. *Dysphagia* 14: 31–42, 1999.
12. **Jung B, Markl M, Foll D, Hennig J.** Investigating myocardial motion by MRI using tissue phase mapping. *Eur J Cardiothorac Surg* 29, *Suppl* 1: 150–157, 2006.
13. **Kahrilas PJ, Logemann JA, Lin S, Ergun GA.** Pharyngeal clearance during swallowing: a combined manometric and videofluoroscopic study. *Gastroenterology* 103: 128–136, 1992.
14. **Lazarus CL, Logemann JA, Pauloski BR, Rademaker AW, Larson CR, Mittal BB, Pierce M.** Swallowing and tongue function following treatment for oral and oropharyngeal cancer. *J Speech Lang Hear Res* 43: 1011–1023, 2000.
15. **Maddock DM, Gilbert RJ.** Quantitative relationship between liquid bolus flow and laryngeal closure during deglutition. *Am J Physiol Gastrointest Liver Physiol* 265: G704–G711, 1993.
16. **Napadow VJ, Chen Q, Mai V, So PTC, Gilbert RJ.** Quantitative analysis of three-dimensionally resolved fiber architecture in heterogeneous skeletal muscle tissue using NMR and optical imaging methods. *Biophys J* 80: 2968–2975, 2001.
17. **Napadow VJ, Chen Q, Wedeen VJ, Gilbert RJ.** Biomechanical basis for lingual tissue deformation during swallowing. *Am J Physiol Gastrointest Liver Physiol* 277: G695–G701, 1999.
18. **Napadow VJ, Chen Q, Wedeen VJ, Gilbert RJ.** Intramural mechanics of the human tongue in association with physiological deformations. *J Biomech* 32: 1–12, 1999.
19. **Napadow VJ, Gilbert RJ.** Three-dimensional muscular architecture of the human tongue visualized in vivo by diffusion tensor magnetic resonance imaging. *Dysphagia* 20: 1–7, 2005.
20. **Napadow VJ, Kamm RD, Gilbert RJ.** A biomechanical model of sagittal tongue bending. *J Biomech Eng* 124: 547–556, 2002.
21. **Nicosia MA, Robbins JA.** The fluid mechanics of bolus ejection from the oral cavity. *J Biomech* 34: 1537–1544, 2001.
22. **Palmer JB, Rudin NJ, Lara G, Crompton AW.** Coordination of mastication and swallowing. *Dysphagia* 7: 187–200, 1992.
23. **Paydarfar D, Gilbert RJ, Poppel CS, Nassab PF.** Respiratory phase resetting and airflow changes induced by swallowing in humans. *J Physiol* 483: 273–288, 1995.
24. **Reese TG, Feinberg DA, Dou J, Wedeen VJ.** Phase contrast MRI of myocardial 3D strain by encoding contiguous slices in a single shot. *Magn Reson Med* 47: 665–676, 2002.
25. **Reichenbach JR, Venkatesan R, Yablonskiy DA, Thompson MR, Lai S, Haacke EM.** Theory and application of static field inhomogeneity effects in gradient-echo imaging. *J Magn Reson Imaging* 2: 266–279, 1997.
26. **Robbins J, Levine R, Wood J, Roecker EB, Luschei E.** Age effects on lingual pressure generation as a risk factor for dysphagia. *J Gerontol A Biol Sci Med Sci* 50: 257–262, 1995.
27. **Smith KK.** Morphology and function of the tongue and hyoid apparatus in Varanus (Varanidae, Lacertilia). *J Morphol* 187: 261–287, 1986.
28. **Smith KK, Kier WM.** Trunks, tongues, and tentacles: moving with skeletons of muscle. *Am Sci* 77: 29–35, 1989.
29. **Stone M, Davis EP, Douglas AS, NessAiver M, Gullapalli R, Levine WS, Lundberg A.** Modeling the motion of the internal tongue from tagged cine-MRI images. *J Acoust Soc Am* 109: 2974–2982, 2001.
30. **Stone M, Epstein MA, Iskarous K.** Functional segments in tongue movement. *Clin Linguist Phon* 18: 507–521, 2004.
31. **Thexton AJ.** Mastication and swallowing. *Br Dent J* 173: 197–206, 1992.
32. **Thexton A, Hiiemae KM.** The effect of food consistency upon jaw movement in the macaque: a cineradiographic study. *J Dent Res* 76: 552–560, 1997.
33. **Thexton AJ, McGarrick JD.** The electromyographic activities of jaw and hyoid musculature in different ingestive behaviors in the cat. *Arch Oral Biol* 39: 599–612, 1994.
34. **Thexton AJ, McGarrick.** Tongue movement of the cat during lapping. *Arch Oral Biol* 33: 331–339, 1988.
35. **Tseng WY, Reese TG, Weisskoff RM, Brady TJ, Wedeen VJ.** Myocardial fiber shortening in humans: initial results of MR imaging. *Radiology* 216: 128–139, 2000.
36. **Wedeen VJ, Reese TG, Napadow VJ, Gilbert RJ.** Demonstration of primary and secondary muscle fiber architecture of the bovine tongue by diffusion tensor magnetic resonance imaging. *Biophys J* 80: 1024–1028, 2001.
37. **Wedeen VJ, Weisskoff RM, Reese TG, Beache GM, Poncelet BP, Rosen BR, Dinsmore RE.** Motionless movies of myocardial strain-rates using stimulated echoes. *Magn Reson Med* 33: 401–408, 1995.
38. **Youmans SR, Stierwalt JA.** Measures of tongue function related to normal swallowing. *Dysphagia* 21: 102–111, 2006.
39. **Zheng X, Pang A.** Volume deformation for tensor visualization. In: *Visualization. Proceeding of the Conference on Visualization 2002*. Washington, DC: IEEE Computer Soc., 2002, p. 379–386.